Iranian Journal of Science & Technology, Transaction B, Engineering, Vol. 33, No. B2, pp 191-206
Printed in The Islamic Republic of Iran, 2009

AUTOMATIC BLOOD VESSEL SEGMENTATION IN COLOR IMAGES OF RETINA*

A. OSAREH** AND B. SHADGAR

Dept. of Computer Science, Shahid Chamran University, Ahvaz, I. R. of Iran
Email: Alireza.Osareh@scu.ac.ir

Abstract– Automated image processing techniques have the ability to assist in the early detection of diabetic retinopathy disease which can be regarded as a manifestation of diabetes on the retina. Blood vessel segmentation is the basic foundation while developing retinal screening systems, since vessels serve as one of the main retinal landmark features. This paper proposes an automated method for identification of blood vessels in color images of the retina. For every image pixel, a feature vector is computed that utilizes properties of scale and orientation selective Gabor filters. The extracted features are then classified using generative Gaussian mixture model and discriminative support vector machines classifiers. Experimental results demonstrate that the area under the receiver operating characteristic (ROC) curve reached a value 0.974, which is highly comparable and, to some extent, higher than the previously reported ROCs that range from 0.787 to 0.961. Moreover, this method gives a sensitivity of 96.50% with a specificity of 97.10% for identification of blood vessels.

Keywords– Retinal blood vessels, Gabor filters**,** support vector machines, vessel segmentation

1. INTRODUCTION

With the fast advances in computing technology, there has been considerable and increasing interest in developing automatic medical diagnosis systems to improve the service provided by the medical community. Reliable and accurate medical diagnosis requires knowledge of changes in different clinical symptoms due to health degeneration and disease deterioration.

The focus of this paper is on the automated identification of blood vessels in color retinal images. These images are taken by making photographs from the back of the eye. We are interested in vessel detection for the purpose of diabetic retinopathy screening. Diabetes is a disease that affects about 5.5% of the population worldwide, a number that can be expected to increase significantly in the coming years [1]. About 10.0% of all diabetic patients have diabetic retinopathy, which is the primary cause of blindness in the working population. Since this type of blindness can be prevented with proper treatment at its early stage, the World Health Organization advises yearly screening of patients. Thus, an automatic system can facilitate this screening process.

The characteristic features of diabetic retinopathy are Microaneurysms, Haemorrhages and Exudates. Microaneurysms are discrete localized distension of the weakened capillary walls and are presented as small, circular red ‘dots’ on the retina. Haemorrhages, or impairments of the blood-retina barrier, appear either as a red ‘dot’ or appear ‘flame-shaped’. In the latter case, they have a characteristically ‘feather-shaped’ edge. Hard exudates are caused by proteins and lipids leaking from the blood into the retina via damaged blood vessels. These appear in retinal images as white or yellow areas, sometimes in a ring-like structure around leaking capillaries.

*Received by the editors November 4, 2007; Accepted July 27, 2008.
**Corresponding author

The main features of a fundus retinal image are defined as the optic disc, fovea and blood vessels. The optic disc is the entrance and exit region of blood vessels to the retina and its localization and segmentation is an important task in an automated retinal image analysis system. Indeed, the fovea corresponds to the region of retina with highest sensitivity.

The blood vessels network is an important anatomical structure in the human retina. Several vascular diseases, such as diabetic retinopathy, have manifestations that require analysis of the vessels network. In other cases, e.g. pathologies like retinal microaneurysms and hemorrhages, the performance of automatic detection methods may be improved if regions containing vessels can be excluded from the analysis [2]. Indeed, the position, size and shape of the vessels provide information which can be used to locate the optic disk and the fovea (central vision area).

So far several methods have been developed for vessel segmentation, but visual inspection and evaluation by ROC analysis shows that there is still room for improvement [3]. In addition, it is important to have algorithms that do not critically depend on configuring many parameters so that untrained community health workers may utilize this technology. These limitations of state of the arts algorithms have motivated the development of the framework described here, which depends on the manually segmented images for training purposes only.

Previous works on blood vessel detection and segmentation can be mainly divided into 3 categories: window-based [4-6], classifier-based [7-11] and tracking-based [12, 13]. Window-based approaches, such as edge detection, estimate a match at each pixel for a given model against the pixel's surrounding window. In [4], the cross section of a retinal vessel was modeled by a Gaussian shaped curve, and then detected using rotated matched filters. In [5] a standard gradient filter was used to detect pixels on the boundaries of vessels for subsequent grouping. In [6], a window surrounding a vessel pixel was modeled by a neural network trained on user-selected examples.

Classifier-based algorithms usually proceed in two steps. First, a low-level algorithm produces a segmentation of spatially connected regions. These candidate regions are then classified as being vessel or not vessel. In [7], regions segmented by a user-assisted threshold were classified as vessel or lesion according to their length to width ratio. In [8], regions segmented by the method [4] were classified as vessel or not, based on many properties, such as their response to a classic operator [14]. In [9] the application of mathematical morphology and wavelet transform was investigated for identification of retinal blood vessels. In a followup work [10], a two dimensional Gabor wavelet was utilized to initially segment the retinal images. A Bayesian classifier was then applied to classify the extracted feature vectors to either vessel or non-vessel class. In [11], three classifiers i.e. *K* nearest neighbor (KNN), linear and quadratic classifiers were utilized to classify the blood vessels. The extracted features were mainly based on the Gaussian and its derivatives up to order 2 at multiple scales.

Tracking-based approaches utilize a profile model to incrementally step along and segment a vessel. In [12], a Hough transform is used to locate the papilla in retinal images. Vessel tracking proceeds iteratively from the papilla, halting when the response to a one-dimensional matched filter falls bellows a given threshold. In [13], the tracking method was driven by a fuzzy model of a one-dimensional vessel profile. One drawback to these approaches is their dependence upon unsophisticated methods for locating the starting points, which must always be either at the optic nerve or at subsequently detected branch points.

In [15-16], blood vessels were detected by means of mathematical morphology. In [17], the a priori distribution of pixel labels is modeled by a Markov random field, and the posterior probability of labeling decisions is maximized by simulated annealing. The effectiveness of these approaches can, however, be affected when the contrast levels between small blood vessels and their background diminish. In [18, 19], matched filters were applied in conjunction with other techniques e.g. genetic algorithms and piecewise thresholding. Another important application of automatic retinal vessel segmentation is in the registration

of retinal images of the same patient taken at different times [20]. In [21], Jiang et al. proposed an adaptive thresholding framework based on verification-based multithreshold probing scheme. Retinal vessels cannot be segmented using a global threshold because of gradients in the background of the image. Instead, Jiang et al. suggested probing the image with different threshold values where at each of the probed thresholds all binary objects in the thresholded image were extracted.

In this paper, we propose a novel vessel segmentation approach to efficiently locate and extract blood vessels in color retinal images. More to the point, this study is concerned with developing fast (computationally efficient) methods while achieving high accuracy. Supervised methods requiring suitable pre-labeled training datasets and with efficient training time can be easily adjusted to new populations. Thus, here we use a Bayesian classifier with class conditional probability density functions described as Gaussain mixtures, yielding a fast classification, while being able to model complex decision surfaces. Our method consists of three major steps: multiscale analysis using Gabor filters, feature extraction based on principal component analysis (PCA), and classifying the image pixels using their corresponding feature vectors by either Gaussian mixture models (*GMMs*) or support vector machines (*SVMs*) classifiers. Finally, the accuracy of our optimum classifiers are evaluated using ROC curves analysis and sensitivity and specificity measurements.

Many of the previously published vessel detection methods have not been evaluated on large datasets or fail to give satisfactory results for large numbers of images as encountered in a routine clinical screening program [22]. As another novelty of this work, we assess the diagnostic accuracy of our proposed method on a large dataset of retinal images comprising 90 normal and abnormal color retinal images. Indeed, in order to compare our proposed method with previous vessel extraction techniques, the efficiency of our method is also validated using a publicly available image dataset i.e. DRIVE which contains 40 retinal images.

In the next section, we will describe the properties of our images, and present a major in-depth review of the algorithm including application of Gabor filters and classification schemes. In Section 3, the experimental evaluation and results are presented and discussed, followed by our conclusions in the last section.

2. MATERIALS AND METHODS

a) Image acquisition

In this work, we have constructed a dataset of 90 images for the training and evaluation of our proposed method. This image dataset was acquired using a Cannon non-mydriatic 3CCD camera (CR6-45NM) with a 45º field of view. Each image was captured using 24 bit per pixel (standard RGB) at 760 x 570 pixels.

Of the 90 images in the dataset, 40 are of patients with no pathologies (normal) and the remaining images contain pathologies (such as microaneurysms, hemorrhages and exudates) that can obscure or confuse the blood vessel appearance in varying positions of the image (abnormal). This selection is made for two reasons. First, most of the referenced methods have only been tested against normal images which are easier to distinguish. Second, some level of success with abnormal vessel appearances must be established to recommend clinical usage. (See Fig. 1 for an example of both a normal and an abnormal retinal image). As can be seen, a normal image consists of blood vessels, optic disc, fovea and the background, but the abnormal image also has multiple artifacts of distinct shapes and colors caused by different diseases.

The image dataset is carefully labeled by an expert to produce ground truth manual vessels segmentation. A typical example of manual segmentation is shown in Fig. 2. The process of labeling an image takes several hours, depending on the expert and image. Overall, the expert marked 13.5% of all pixels as vessel based on our image dataset of 90 retinal images.

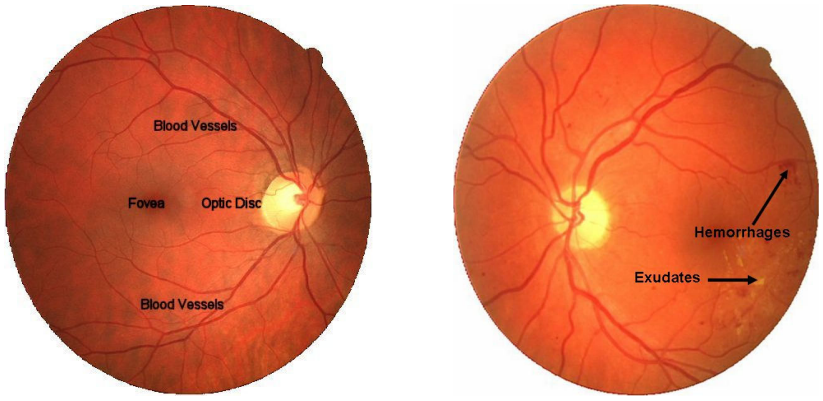

(a) (b)

Fig. 1. Digital retinal images. a) a normal image from our image dataset shows blood vessels, optic disc and fovea components, b) an abnormal image with exudate and hemorrhage lesions

b) Pixel-level learning dataset building

In this work**,** the image pixels of the retinal images are considered as objects represented by their feature vectors, so that we can apply statistical classifiers in order to classify the image pixels. Here, we assume a binary multi-dimensional classification approach to distinguish the vessel pixels from other anatomical-pathological structures and artifacts, which we refer to collectively as non-vessels. Our chosen data for the learning stage consists of typical pixels, which are representative of our classification problem. To make-up such a dataset, examples, including vessels and non-vessels are labeled manually and then used to train and test the classifiers (Fig. 2). The obtained labeled examples (feature vectors) are mapped into the feature space, and their labels are utilized to obtain those subspaces which correspond to our two different classes i.e. vessel and non-vessel.

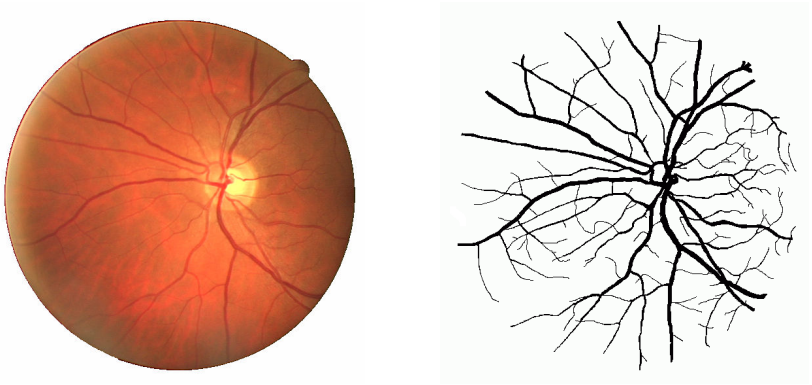

(a) (b)

Fig. 2. Manual blood vessel segmentation. a) A typical normal image, b) manually segmented vessels

A nearly balanced learning dataset of vessel and non-vessel pixels was established to eliminate any possible bias towards either of the two classes. Our representative learning dataset is comprised of 250000 vessel and 251000 non-vessel pixels.

c) Two dimensional Gabor filters

Gabor filters have been broadly used for multi-scale/multi-directional analysis in image processing. These filters have specifically shown high performance as feature extractors for discrimination purposes [23, 24]. Due to Gabor filters directional selectiveness capability in detecting oriented features and fine tuning to specific frequencies and scale, these filters act as low-level oriented edge discriminators and are especially important in filtering out the background noise of the images.

Mathematically, a two-dimensional (2D) Gabor function, *g*, is the product of a 2D Gaussian and a complex exponential function which in general form is given by:

$$g_{\theta,\lambda,\sigma_1,\sigma_2}(x,y) = \exp\left\{-\tfrac{1}{2} M (x,y)^T\right\} \exp\left\{\frac{j\pi}{\lambda}(x\cos\theta + y\sin\theta)\right\} \quad (1)$$

Where $M = diag(\sigma_1^{-2}, \sigma_2^{-2})$. The parameter θ represents filter orientation, λ is the filter wavelength which modifies the sensitivity to high/low frequencies, and σ_1 and σ_2 characterize the filter standard derivations which represent scale value at orthogonal directions. However, with this parameterization, the Gabor function does not scale uniformly when σ changes. Thus, it is preferable to use a new parameter $\gamma = \lambda/\sigma$ instead of λ, so that a change in σ corresponds to a true scale change in the Gabor function. Also, it is more convenient to apply a 90 degree counterclockwise rotation, such that θ expresses the orthogonal direction to the Gabor function edges. Now, the Gabor functions can be defined as follows:

$$g_{\theta,\gamma,\sigma}(x,y) = \exp\left\{-\frac{x^2 + y^2}{2\sigma^2}\right\} \exp\left\{\frac{j\pi}{\gamma\sigma}(x\sin\theta - y\cos\theta)\right\} \quad (2)$$

By convolving a Gabor function $g_{\theta,\gamma,\sigma}$ with image patterns *f(x,y)*, we can evaluate their similarities. Here, we define the Gabor response at the point (x_0, y_0) as follows:

$$G_{\theta,\gamma,\sigma}(x_0,y_0) = (f * g_{\theta,\lambda,\sigma})(x_0,y_0) = \int f(x,y) g_{\theta,\gamma,\sigma}(x_0 - x, y_0 - y)\,dxdy \quad (3)$$

where * represents convolution. In Fig. 3, we illustrate the variation of parameters (γ, θ, σ) in the shape of the Gabor function.

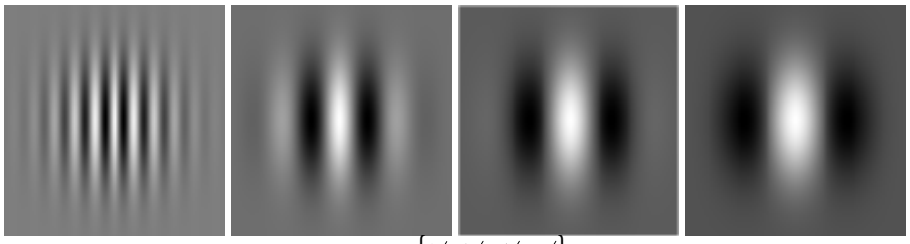

(a) $\gamma = \{1/2, 3/2, 5/2, 7/2\}$

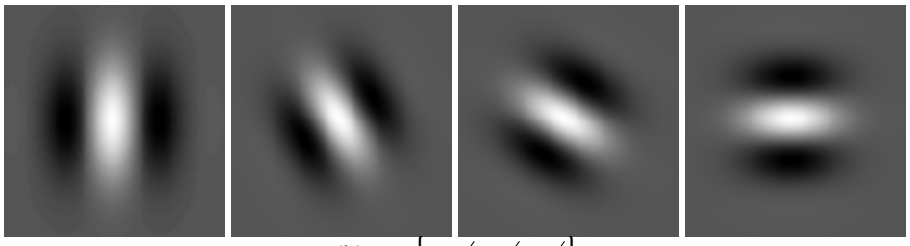

(b) $\theta = \{0, \pi/6, \pi/3, \pi/2\}$

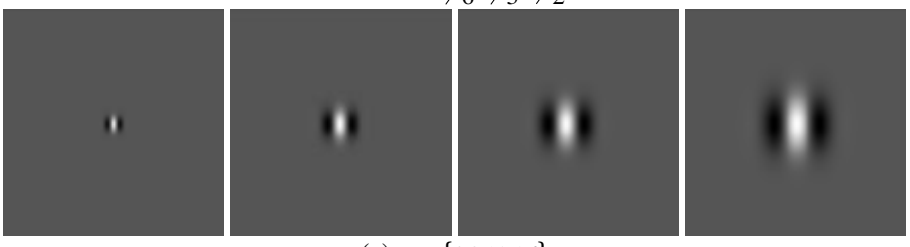

(c) $\sigma = \{4,8,12,16\}$

Fig. 3. Examples of Gabor functions. Each sub figure shows the real part of Gabor function for different values of a) γ, b) θ, and c) σ

There are two major ways to optimally choose the parameters of a Gabor filter i.e. *supervised* and *unsupervised*. In a supervised manner, several sets of parameters are tried to find out the optimum filter (or a few filters) for a given problem. Whereas in an unsupervised approach, a filter bank which spreads throughout the frequency plane can be used. The unsupervised method is more general and more popular; however dealing with a filter bank means a higher computational cost and a larger feature space [25].

Here, in order to tune the Gabor filter response to particular patterns such as blood vessels, it is necessary to adjust Gabor filter bank parameters, namely orientations, frequencies/wavelengths, and scales properly. This issue will be discussed in more detail in the next section.

d) Feature extraction and normalisation

When the RGB components of the retinal images are visualized separately, the green channel represents the best vessel-background contrast, whereas the red and blue channels are low contrast and noisy. Thus, the green channel was selected to be processed by the Gabor filters. Moreover, before the application of the Gabor filters to images, we invert the green channel of the image so that the vessels appear brighter than the background.

In order to initially locate the blood vessels from the retinal images we used a Gabor filter bank $G_{\theta,\gamma,\sigma}$ arranged in 12 orientations (θ spanning from 0^o up to 165^o at steps of 15^o), 3 wavelengths (γ = 1.5, 2.5, 3.5) and 3 scales ($\sigma = 3,5,7$). The wavelength and scale values were experimentally tuned according to our prior knowledge of retinal image characteristics and in such a way to assign stronger responses to pixels associated with the blood vessels of all possible widths. The response of such a filter bank to an input image is a set of filtered images. In fact, for each considered set of wavelengths and scale parameters, we were interested in the Gabor filter response with the maximum value over all possible orientations. These maximum values were then taken as the main components of the pixel feature vectors. Figure 4 shows a typical retinal image and its corresponding maximum Gabor filter response for 2 different scale values. Having primarily extracted the candidate blood vessels network based on Gabor filter responses, the filtered image pixels were then classified in terms of vessels and non-vessels.

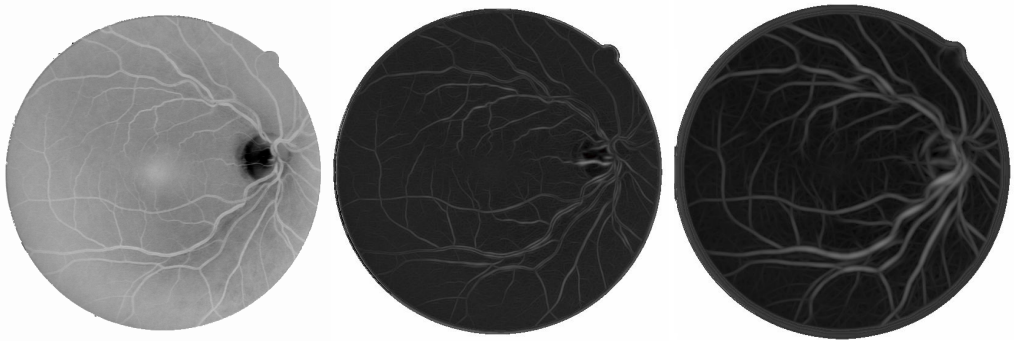

(a) (b) (c)

Fig. 4. Gabor filters taking the maximum response for all orientations $\theta = 0^o$ up to 165^o at steps of 15^o. a) Inverted green channel of a typical retinal image, b) maximum Gabor filter response values with γ=2.5, σ=1, c) maximum Gabor filter response values with γ=2.5, σ=5

To improve the discrimination ability of the classifiers, contextual information is utilized. To do that, an odd-sized square window was centered on each underlying pixel x_0 in the original image. Then the L*uv* color components [26] of the pixels in the window (in an 8-connectivity manner) were composed into the feature vector of x_0. There might be no constraint on the neighborhood window size in theory, but it is assumed that most contextual information is presented in a small neighborhood of the x_0 pixel. Thus the window must be chosen large enough to contain blood vessels, but small enough to avoid potential interference from the neighboring non-vessel pixels.

A small window size is also favorable for computational reasons. In this study, to determine the optimal window size, we examined various window sizes and obtained the best results with a 3x3 window. The total number of features for each typical image pixel was therefore 3x3+9x3=36, comprising 9 maximum Gabor filtered responses (3x3) and 27 L*uv* color components of the 9 pixels (9x3) in the considered local window. This resulted in a computationally demanding high dimensional feature space. Thus, we used a feature extraction approach to obtain a lower dimensional feature space, combating the curse of dimensionality while retaining sufficient accuracy of representation. A limited by prominent feature set can simplify both the vessels representation and the classifiers that are built on the selected features. Therefore, the designed classifier will be faster and require less memory.

We defined dimensionality reduction as the transformation of a p dimensional vector x_i^p to a q dimensional vector x_j^q, where $q << p$ using the PCA technique. The PCA began by computing the mean of feature vectors x^n and then subtracting the means off [27]. The covariance matrices were evaluated next and then we calculated the eigenvectors and eigenvalues of the covariance matrices for vessels and non-vessels. The output of the PCA was a set of eigenvectors and eigenvalues, with the eigenvalues representing the amount of variance over the whole dataset of pixels for each vector. A central issue in PCA is choosing the number of principal components to be retained. Here, we conducted an experiment and projected our chosen pixel dataset onto the subspace of the principal components which accounted for more than 95% of the total variance. The first 15 vessel eigenvalues contained 95.1% of total variance, whereas the first 21 non-vessel eignvalues captured 95.6% of the total variance.

Given the dimensional nature of the new features now forming the feature space, this might cause errors in the classification process, as the units chosen might affect the distance in the feature space. A new way to obtain a new random variable with zero mean and unit standard deviations, yielding, in addition, dimensionless features, is to apply the normal transformation to the feature space as follows:

$$\bar{x}_j = \frac{x_j - \mu_j}{\sigma_j} \tag{4}$$

where x_j is the j^{th} feature assumed by each pixel, μ_j is the average value of the j^{th} feature and σ_j is the associated standard deviation.

e) Supervised pixel-level blood vessel classification

Machine learning-based classification methods provide a formal approach for manipulating nondeterministic models by describing or estimating a probability density over the variables in question. Within this generative density, one can specify a priori partial knowledge and refine the partially specified model using empirical observations and data [28]. Thus, given a system with variables $x_1, \ldots, x_T$, this system can be specified through a joint probability distribution over all the significant variables within it $p(x_1, \ldots, x_T)$. This is known as a generative model since given this probability distribution; we can generate samples of various configurations of the system.

Ironically, the flexible generative models have been recently outperformed in many cases by relatively simpler models estimated with discriminative algorithms. Unlike a generative modeling approach where modeling tools are available for combining structure, priors, variables and data to form a good joint density tailored to the domain at hand, discriminative algorithms directly optimize a relatively less domain-specific model for the classification or task at hand. For example, support vector machines [29-30] directly maximize the margin of a separator between two sets of points in an Euclidean space.

In this study, we analyzed the performance of several classifier models to select the one with the most accurate results. Here, we chose one very commonly used model for every type of generative and discriminative based approach, i.e. Gaussian mixture model and support vector machines towards our pixel-level blood vessel recognition task.

Following the learning stage and tuning the model parameters, each classifier was quantitatively evaluated by independent unseen test sets; otherwise the evaluation would become biased and would not represent a fair assessment of the classifier performance. To assess the classifier generalisation ability and thus measure the classification error, a 5-fold cross validation technique was employed [27]. Moreover, to have a fair comparison between different classifiers, the training and validation descriptions were kept constant for all classification experiments, which are described in the next two sections.

1. Mixture model classification: GMM classifiers have been utilized in various applications of computer vision and medical imaging [31]. They are widely used in applications where data can be viewed as a combination of different populations mixed in varying proportions. Basically, in a mixture model distribution, the data density is represented as a linear combination of component densities in the form:

$$p(x) = \sum_{k=1}^{K} p(x_i \mid w_k; \Theta_k) P(w_k) \tag{5}$$

where K represents the number of components and each component is defined by w_k and parameterised by Θ_k (mean and covariance density function parameters). The coefficient $P(w_k)$ is called the mixing parameter and corresponds to the prior probability that the d-dimensional feature vector x is generated by the component k. We benefited from the theory behind these models and used two separate mixtures of Gaussians to estimate the class densities $p(x|C_i, \Theta)$ of vessels and non-vessels, as follows:

$$p(x \mid C_i, \Theta) = \sum_{k=1}^{K_i} \frac{P(w_k)}{(2\pi)^{\frac{d}{2}} \det(\sum_k)^{\frac{1}{2}}} \exp\left\{-\frac{1}{2}(x-\mu_k)^T \sum_k^{-1} (x-\mu_k)\right\} \tag{6}$$

μ_k and $\sum_k$ denote the mean and covariance of the k^{th} component of the mixture density of class C_i. K_i denotes the number of components in class i, and C_i refers to either the vessel or non-vessel class. The final decision regarding the class affiliation of each new feature vector x was taken using Bayes rule [27].

Various procedures have been developed to determine the parameters of a *GMM* ($\Theta = \{\mu_k, \sum_k, P(w_k)\}$). The Expectation Maximisation (EM) algorithm is the one most widely used [29]. This algorithm consists of two major steps: the Expectation (E-step) and the Maximisation (M-step). The EM algorithm requires an initialization step which assigns primary values to the model's parameters. These primary values have an essential effect on the algorithm's convergence and the obtained accuracy. Here, these parameters are initialised using a K-means clustering algorithm [32].

K-means algorithm has an important parameter i.e. K (number of clusters) which needs to be defined beforehand. We will return back to this issue in the next section. Indeed, we need to decide on the form of the component densities or equivalently the form of the component covariance matrices. Basically, three different forms of covariance matrices can be defined for the mixture components i.e. spherical, diagonal and full [33]. Here, we assume a full covariance matrix for each mixture component, since these types of matrices have higher flexibility in estimating the underlying distributions.

After these initialisation settings, the K-means clustering is iteratively applied for 20 iterations. The mixing parameters are computed from the proportion of examples belonging to each cluster. Having estimated the location of the component centres, the covariance matrices are then calculated as the sample covariance of the points associated with the corresponding centres. Then the EM algorithm is then iterated for 30 iterations, which is enough for convergence in our application.

It is worth noting that all described steps are applied separately on vessel and non-vessel pixel datasets and then the two estimated distributions are unified through a maximum, a posterior decision rule [34]. Experimental results follow in section 3 to demonstrate the accuracy of the proposed classification

scheme. Before that we describe a procedure for the selection of the optimum number of *GMM* components.

-Selection of optimum number of components: The number of mixture components (K) in *GMMs* relies on a combination of good modeling, a sensible number of parameters, and avoidance of a highly complex model. Choosing too few mixture components produces a model that cannot accurately model the vessels and non-vessels. With an increasing number of components, the probability that the model fits the dataset better will be increased, but the model will also lose its capability to generalise well. In this work, the appropriate number of components was chosen by repeating the density model estimation and evaluating a criterion by varying the number of components. The evaluation measurement was the Minimum Description Length (MDL) principle [35]. The appropriate number of components can be found using the following formula:

$$MDL(K) = -\ell og(\Theta) + \frac{1}{2}\upsilon(K)\log N \tag{7}$$

Where $-\ell og(\Theta)$ shows the pixel data log likelihood, N refers to the total number of data points and $\upsilon(K)$ denotes the mixture model dimension or the number of free parameters in a mixture model. There are $d(d+1)/2$ free parameters for each full covariance matrix component where d is the dimensionality of the feature space. Each mean vector μ has d free parameters and the mixing parameters $P(w_k)$ require another K-1 parameter. Thus, the dimension of a *GMM* is written as:

$$\upsilon(K) = K\left(\frac{d(d+1)}{2} + d\right) + K - 1 \tag{8}$$

The selection of an optimal number of components, i.e. $\overline{K}$, is performed by choosing the argument K that minimises Eq. (7). In this work, by varying the number of components within a range of 1 to 15 we could acquire the optimum number of mixture components (K) for our vessel and non-vessel pixel datasets separately. These were 5 and 8 components for vessel and non-vessel pixel datasets, respectively. Figure 5 illustrates the MDL values for both vessel and non-vessel pixel datasets. A trend seen from Fig. 5 suggests a higher number of components for estimating the non-vessel distribution compared to the vessels. This could be due to the greater variability which existed amongst the non-vessel sample points.

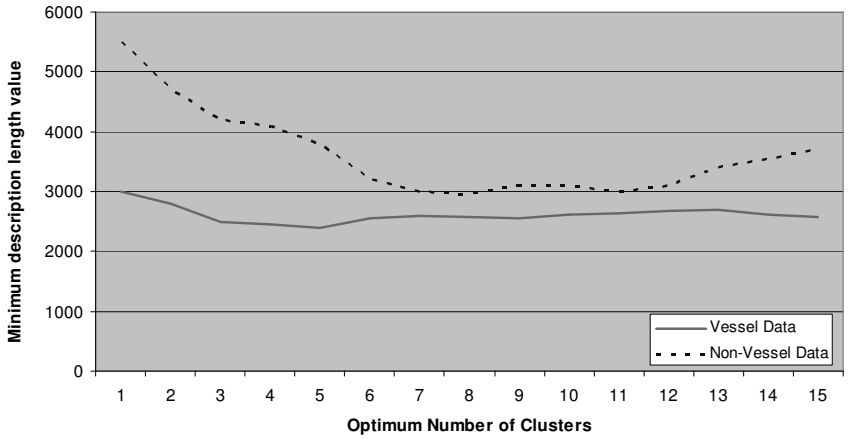

Fig. 5. Minimum description length value of vessel and non-vessel pixel datasets for choosing appropriate number of clusters

2. Support vector machines classification: Discriminative *SVMs* have become an increasingly popular tool for machine learning tasks involving classification and regression [30]. Here, we investigate the *SVMs* application to our medical decision support task of classifying the retinal image pixels to vessel and non-vessel classes. The *SVMs* demonstrate various attractive features such as good generalisation ability compared to other classifiers. Indeed, there are relatively few free parameters to adjust and it is not required to find the architecture experimentally.

The *SVMs* algorithm separates the classes of input patterns with the maximal margin hyperplane. This hyperplane is constructed as:

$$f(x) = \langle w, x \rangle + b \tag{9}$$

where x is the feature vector, w is the vector that is perpendicular to the hyperplane, and $b\|w\|^{-1}$ specifies the offset from the beginning of the coordinate system. To benefit from non-linear decision boundaries, the separation is performed in a *feature space F*, which is introduced by a nonlinear mapping φ of the input patterns. This mapping is defined as follows:

$$\langle \varphi(x_1), \varphi(x_2) \rangle = K(x_1, x_2) \qquad \forall x_1, x_2 \in \mathrm{X} \tag{10}$$

for some *kernel function* $K(\cdot, \cdot)$. The kernel function represents the non-linear transformation of the original feature space into the F. However, to guarantee that the resultant hyperplane separates the classes, the following constraints must be satisfied:

$$y_i.(\langle w, x_i \rangle + b) \geq 1 - \xi_i, \qquad \xi_i \geq 0, \qquad i = 1,...n \tag{11}$$

where $y_i \in \{-1,1\}$ denotes the class label corresponding to the input pattern $\boldsymbol{x}_i$. The variables ξ_i are utilized to allow for the training of the classifier on linearly non-separable classes. The slack variables must be penalized in the minimization term. Consequently, the learning of the *SVMs* classifier is equivalent to solving a minimization problem with the objective function of the form:

$$\min_{w \in \mathrm{X}} \frac{1}{2}\|w\|^2 + C\sum_{i=1}^{n} \xi_i \tag{12}$$

The penalty C is a regularization parameter that controls the trade-off between maximizing the margin and minimizing the training error. This approach is called soft margins [30]. Using the Lagrange multiplier technique, we can transform this optimization problem to a dual form:

$$\min_{\alpha \in R^n} \sum_{i=1}^{n} \alpha_i - \frac{1}{2}\sum_{i,j}^{n} \alpha_i \alpha_j y_i y_j . K(x_i, x_j) \tag{13}$$

subject to:

$$0 \leq \alpha_i \leq C \qquad \sum_{i=1}^{n} \alpha_i y_i = 0 \tag{14}$$

In the above formulation, the $\alpha = \{\alpha_1, \alpha_2, ...\alpha_n\}$ is the vector of Lagrange multipliers. The Lagrange multipliers that solve the Equation (13) can be used to compute the decision function:

$$f(x) = \sum_{i=1}^{n} \alpha_i y_i K(x_i, x) + b \tag{15}$$

where

$$b = y_i - \sum_{j=1}^{n} \alpha_j y_j K(x_j, x_i) \tag{16}$$

3. EXPERIMENTAL EVALUATION AND RESULTS

The performance of a medical diagnosis system is best described in terms of *sensitivity* and *specificity.* These criteria quantify the system performance according to the *false positive* (*FP*) and *false negative* (*FN*) instances. The sensitivity gives the percentage of correctly classified abnormal cases while the specificity defines the percentage of correctly classified normal cases.

Here, the performance of the selected *GMMs* was quantified based on its *sensitivity*, *specificity* and the *overall accuracy* (fraction of correctly classified pixels).The best overall classification accuracy obtained was 95.24%, with 96.14% sensitivity and 94.84% specificity based on the optimum number of components.

Alternatively, we classified our manual segmented vessel and non-vessel pixels dataset using *SVMs* with a different number of kernels and parameters. Specifying a *SVM*s classifier requires two parameters: the *kernel function* and the *regularization parameter C*. In this study, the *SVMs* classifiers were evaluated independently for the following three kernel functions:

- Linear kernel: $K(x, y) = \langle x, y \rangle$
- Polynomial kernel of order 4: $(\sigma(x, y) + \gamma)^4$
- Gaussian radial basis function (RBF) kernel: $e^{-\|x-y\| / 2\sigma^2}$

In order to obtain the optimal value for the *SVMs* regularization parameter *C* and parameters of kernel functions, we experimented with different *SVMs* classifiers for a range of values using a 5-fold cross validation technique. The performance of the selected *SVMs* was again measured based on its *sensitivity, specificity* and the *overall accuracy.* In the first experiment, with no restrictions on the Lagrange multipliers (hard margin), we achieved an optimum overall accuracy of 94.45% with 93.42% sensitivity and 95.51% specificity for σ=2.5 using a RBF kernel.

Figure 6a illustrates the generalization performance of the optimum classifier against varying values of σ in each case. This classifier represents a good performance over vessel and non-vessel cases. The obtained classification accuracies for different kernel functions are presented in Table 1. As is evident, the highest accuracy in both hard margin and soft margin cases was achieved when using the Gaussian RBF kernel.

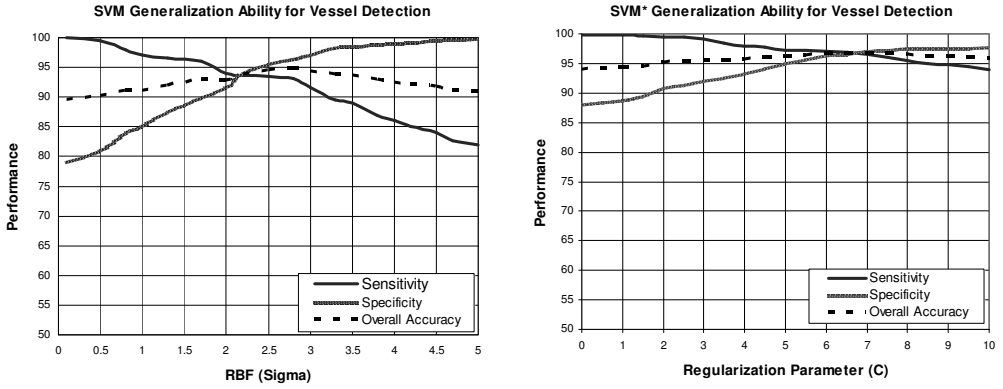

(a) (b)

Fig. 6. Generalization performance of the Gaussian RBF *SVMs* classifiers against a) different σ values, b) different *C* values

In the second experiment, to illustrate the effect of the soft margins approach, we evaluated the generalization ability of the different *SVMs* classifiers on the training set with σ fixed at 2.5 and for a wide range of *C* values which were applied as an upper bound to α_i (Fig. 6b). Afterwards, for each of the kernel

functions we selected the value of regularization parameter C that yielded the highest classification accuracy. Using the same approach we selected the values for the γ parameter.

Table 1. Optimum values of kernels and regularization parameters used in *SVMs* classifiers

	Kernel function	Kernel parameters	Regularization parameter C	Sensitivity	Specificity	Overall accuracy
Hard Margins	Linear	-	-	93.04 %	92.15 %	93.34 %
	Polynomial	$\sigma = 0.9$ $\gamma = 0.2$	-	94.87 %	92.18 %	93.60 %
	RBF	$\sigma = 2.5$	-	93.42 %	95.51 %	94.45 %
Soft Margins	Linear	-	$C = 5.3$	93.15 %	93.90 %	94.55 %
	Polynomial	$\sigma = 0.9$ $\gamma = 0.2$	$C = 8.1$	94.11 %	95.00 %	94.02 %
	RBF	$\sigma = 2.5$	$C = 7.0$	96.50 %	97.10 %	96.75 %

The results of the parameter study are summarized in Table 1. As can be seen, the best overall accuracy, using the soft margins technique (referred to as *SVM**), increased to 96.75% with 96.50% sensitivity and 97.10% specificity at C=7.0 based on a Gaussian RBF kernel.

Table 2 summarizes both *GMM* and *SVMs* results. These are the best results from a selection of configurations used for training the classifiers. Although the diagnostic accuracy of the *SVM** classifiers is slightly better than the *GMMs*, the classifier performances are very close and there is a good balance between sensitivity and specificity in both cases.

Table 2. Performances of optimum classifiers for blood vessel pixels classification

Classifier	Sensitivity	Specificity	Overall accuracy	*Az*
GMM with 5 vessel and 13 non-vessel components	96.14 %	94.84 %	95.24 %	0.965
*SVM** $\sigma = 2.5$, $C = 7.0$	96.50 %	97.10 %	96.75 %	0.974

In most medical applications the *overall accuracy* may not be a sufficient measure to choose the optimal configuration. Thus, in order to assess and analyze the behavior of the optimum classifiers throughout a whole range of the output threshold values, ROC [36] curves shown in Fig. 7 have also been produced (with true-positives plotted against the false-positives describing the tradeoff between sensitivity and specificity). The bigger the area under the ROC curve (A_z), the higher the probability of making a correct decision. Therefore, A_z can be used as a single measure of the performance of each method.

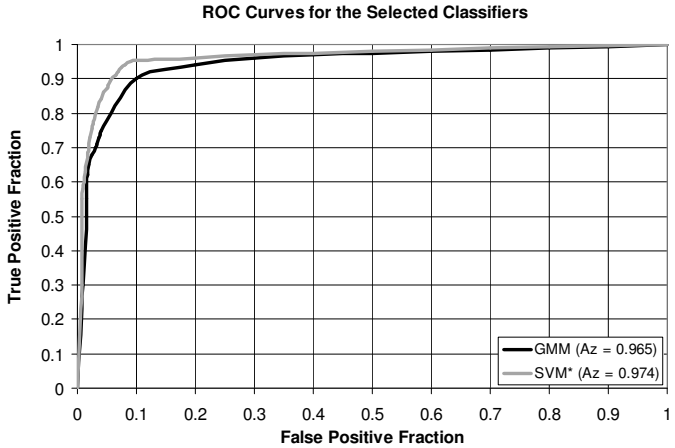

Fig. 7. ROC curves for blood vessel pixels classification using classifiers in Table 2.

Here, both *GMM* and *SVM** classifiers achieved high performances with areas 0.965 and 0.974, respectively (Table 2). However, as Fig. 7 illustrates, the *SVM** classifier shows, to some extent, a higher performance over the entire ROC space.

So far we have discussed pixel-level classification. We can use our trained classifiers to evaluate the effectiveness of our proposed approach by assessing the whole image pixels. To do this, we considered a population of 40 (20 normal and 20 abnormal) new unseen retinal images. Each image was evaluated using the *SVM** classifier and a final decision was made to discriminate the vessel pixels. The classification result for each image pixel was a real value and these values were then utilized to create the final classified images. Figure 8 illustrates two typical normal retinal images and an abnormal image from our image dataset that have been classified at pixel-level using the optimum *SVM** classifier. The original images, ground-truths and the final identified blood vessels are shown in this figure.

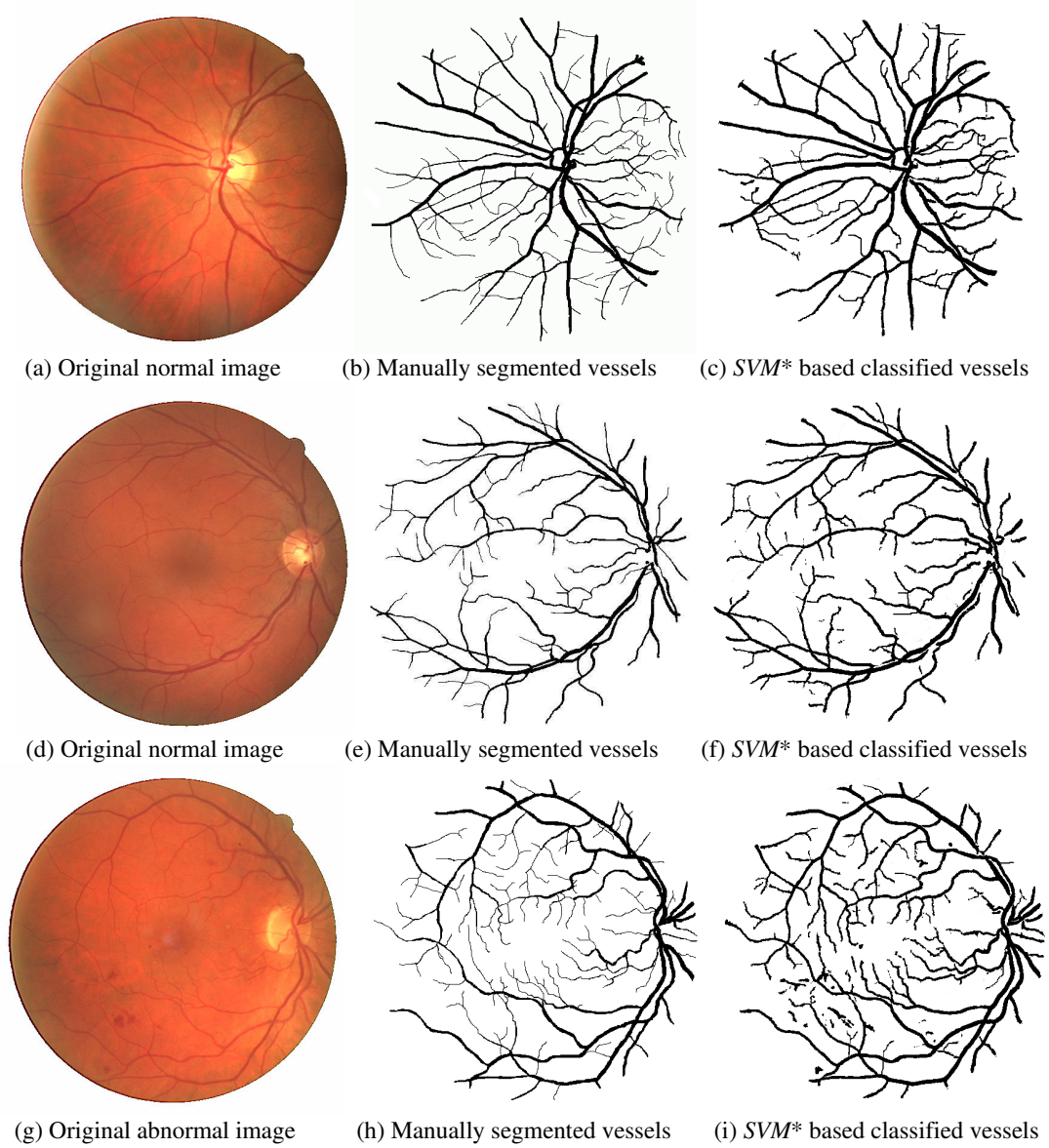

(a) Original normal image (b) Manually segmented vessels (c) *SVM** based classified vessels

(d) Original normal image (e) Manually segmented vessels (f) *SVM** based classified vessels

(g) Original abnormal image (h) Manually segmented vessels (i) *SVM** based classified vessels

Fig. 8. Retinal blood vessel pixel classification results produced by the optimum *SVM** classifier for typical normal and abnormal images

As is evident from Fig. 8, our proposed vessel segmentation algorithm could locate and extract the blood vessels effectively (Fig. 8 (c, f, i)). Although, the majority of large and small vessels are detected, there is some erroneous false detection of noise and other artifacts. The major errors are due to background noise and non-uniform illumination across the retinal images, border of the optic disc and other types of pathologies (such as false positive pixels in Fig. 8(i)) that present strong contrasts. Another difficulty is the lack of precision to capture some of the thinnest vessels that are barely perceived by human observers. In fact, small retinal vessels usually have poor local contrast and they almost never have ideal solid edges.

In order to compare our results with the most related works in the literature, the publicly available benchmark DRIVE dataset [22] was also used for evaluating the performance of the presented method. This database contains 40 images in which the blood vessel structures have been manually segmented. Here, the performances of five different algorithms which have all been evaluated using this dataset are compared. These are Chandhuri et al. [4], Soares et al. [10], Niemeijer et al. [11], Zang et al. [20] and Jiang et al. [21]. Table 3 shows an overview of the results for different methods in terms of the area under the ROC curve (A_z). As is evident, the area under the ROC curve for our method reached a value 0.965 which is highly comparable and slightly higher than the best previously reported accuracies that range from 0.787 to 0.961.

Table 3. Comparison of our proposed technique against past five vessel identification methods

Blood vessel identification method	*Az*
Chandhuri	0.787
Soares	0.961
Niemeijer	0.929
Zang	0.898
Jiang	0.911
Our method	0.965

A possible explanation for the fact that the pixel classification outperforms the other methods is that the Soares, Niemeijer and our method are the only supervised methods (i.e. trained with examples). For a segmentation problem as complicated as the one at hand it is very hard to establish rules which work in all types of situations that can occur in a large set of images.

The proposed segmentation algorithm was performed on a 3.4 GHz PC with 2GB RAM. All implementations are in Matlab and there is room for optimizations. Indeed, our *SVM* based classifier was trained using only 50000 training pixels (from DRIVE images) instead of the 1 million used by Soares et al. [10]. Thus, our method significantly lowered the training time (about 45 minutes compared to the 9 hours) with an average image classification time around 30 seconds. Therefore, the presented algorithm is more suitable when the system needs to be adapted for new datasets and also tends to generalize well when applied to data outside the training set.

4. CONCLUSION

In this paper, we present a novel automatic blood vessel detection algorithm for retinal images acquired from diabetic retinopathy screening programs. The results we have obtained suggest that pixel-level classification in conjunction with Gabor filter responses, feature extraction and *SVMs* classifiers can provide robust and computationally efficient blood vessel segmentation while suppressing the backgrounds.

Through a comprehensive optimization process of operational parameters, our proposed scheme does not require any user intervention, and it has consistent performance for both normal and abnormal images.

The results by the two classification approaches i.e. *GMM* and *SVMs* are very similar; however, we believe that *SVMs* are a more practical solution to our application as they always converge to the same solution for a given dataset regardless of initial conditions, and finally, they remove the danger of overfitting.

Our experimental results show that the area under the ROC curve reached a value of 0.974 against a retinal image dataset comprising 90 normal and abnormal images. Indeed, our method achieves a sensitivity of 96.50% with a specificity of 97.10% for identification of blood vessels. In a second experiment, to compare our results with previous state of the art works, the publicly available benchmark DRIVE dataset was also used for evaluating the performance of the presented method. Using this dataset, the area under the ROC curve for our method reached a value of 0.965, which is highly comparable and slightly higher than the best previously reported accuracies that range from 0.787 to 0.961. Moreover, the presented method proved to be computationally efficient with an average image classification time around 30 seconds.

Using this method, eye care specialists can potentially monitor larger populations for vessel abnormalities and other diseases. Indeed, observations based upon such a tool would also be more systematically reproducible.

REFERENCES

1. Klein, R., Klein, B., Moss, S., Davis, M. & Demets, D. (1984). The Wisconsin epidemiologic study of diabetic retinopathy II. Prevalence and risk of diabetic retinopathy when age at diagnosis is less than 30 years. *Archives of Ophthalmology*, Vol. 102, pp. 520-526.
2. Early treatment diabetic retinopathy study research group. (1991). Early photocoagulation for diabetic retinopathy: ETDRS Report 9. *Ophthalmology*, Vol. 98, pp. 766-785.
3. Cree, M., Leandro, J., Soares, J. & Jelinek, H. (2005). Comparison of various methods to delineate blood vessels in retinal images. *Proc. of the 16th National Congress of the Australian Institute of Physics*, Canberra, Australia, pp. 17-25.
4. Chaundhuri, S., Chatterjee, S., Katz, N., Nelson, M. & Goldbaum, M. (1989). Detection of blood vessels in retinal images using two-dimensional matched filters. *IEEE Trans. on Medical Imaging*, Vol. 8, No. 3, pp. 263-269.
5. Pinz, A., Bernogger, S., Datlinger, P. & Kruger, A. (1998). Mapping the human retina. *IEEE Trnas. on Medical Imaging,* Vol. 17, No. 4, pp. 606-619.
6. Nekovei, R. & Sun, Y. (1995). Back propagation network and its configuration for blood vessel detection in angiograms. *IEEE Trans. on Neural Networks,* Vol. 6, No. 1, pp. 64-72.
7. Tamura, S., Tanaka, K., Ohmori, S. & Hoshi, M. (1983). Semiautomatic leakage analyzing system for time series fluorescein ocular fundus angiopraghy. *Pattern Recognition,* Vol. 16, No. 2, pp. 149-162.
8. Cote, B., Hart, W., Goldbaum, M., Kube, P. & Nelson, M. (1994). Classification of blood vessels in ocular fundus imgaes, technical report. *Computer Science and Engineering Dept, University of California*.
9. Leandro, J., Cesar, R., & Jelinek, H. (2001). Blood vessels segmentation in retina: Preliminary assessment of the mathematical morphology and the wavelet transform techniques. *Proc. Of the 14th Brazilian Symposium on Computer Graphics and Image Processing*, pp. 84-90.
10. Soares, J., Leandro, J., Cesar, R., Jelinek, H., & Cree, M. (2006). Retinal vessel segmentation using the 2-D Gabor wavelet and supervised classification. *IEEE Trans. on Medical Imaging*, Vol. 25, No. 9, pp. 1214-1222.
11. Niemeijer, M., Staal, J., Ginneken, B., Loog, M. & Abramoff, M. (2004). Comparative study of retinal vessel segmentation methods on a new publicly available database. *SPIE Medical Imaging*, Vol. 5370, pp. 648-565.
12. Tamura, S., Okamoto, Y. & Yanashima, K. (1988). Zero-crossing interval corrections in tracing eye-fundus blood vessels. *Pattern Recognition,* Vol. 21, No. 3, pp. 227-233.

13. Tolias, Y. & Panas, S. (1998). A fuzzy vessel tracking algorithm for retinal images based on fuzzy clustering. *IEEE Trnas. on Medical Imaging,* Vol. 17, 2,pp. 263-273.
14. Fischer, M., Tenenbaum, J. & Wolf, H. (1981). Detection of roads and linear structures in low resolution aerial imagery using a multisource knowledge integration technique. *Computer Graphics and Image Processing,* Vol. 15, No. 3, pp. 201-223.
15. Jasiobedzki, P., Mcleod, D. & Taylor, C. (1991). Detection of non-perfused zones in retinal images. *Computer-Based Medical Systems: Fourth Annual IEEE Symposium*, pp. 162-169.
16. Zang, F. & Kelin, J. (2001). Segmentation of vessel like patterns using mathematical morphology. *IEEE Trans. on Medical Imaging,* Vol. 10, No. 7, pp. 1010-1019.
17. Simo, A. & de Ves, E. (2001). Segmentation of macular fluorescen angiographies, a statistical approach. *Pattern Recognition,* Vol. 34, No. 4, pp. 795-809.
18. Al-Rawi, M. & Karajeh, H. (2007). Genetic algorithm matched filter optimization for automated detection of blood vessels from digital retinal images. *Computer Methods and Programs in Biomedicine*, Vol. 87, pp. 248-253.
19. Hoover, A., Kouznetsov, V. & Goldbaum, M. (2000). Locating blood vessels in retinal images by piecewise threshold probing of a matched filter response. *IEEE Trans. on Medical Imaging,* Vol. 19, No. 3, pp. 203-210.
20. Zang, F. & Klein, J. (1999). A multimodal registration algorithm of eye fundus images using vessels detection and Hough transform. *IEEE Trans. on Medical Imaging,* Vol. 18, No. 5, pp. 419-428.
21. Jiang, X. & Mojon, D. (2003). Adaptive local thresholding by verification-based multithreshold probing with application to vessel detection in retinal images. *IEEE Trans. on Pattern Analysis and Machine Intelligence*, Vol. 25, No. 1, pp. 131-137.
22. Staal, J., Abramoff, M., Niemeijer, M. & Viergever, M. (2004). Ridge-based vessel segmentation in color images of retina. *IEEE Trans. on Medical Imaging,* Vol. 23, No. 4, pp. 501-509.
23. Drimbarean, A. & Whelan, P. (2001). Experiments in color texture analysis. *Pattern Recognition Letters*, Vol. 22, No. 10, pp. 1161-1167.
24. Nestares, O., Navarro, R., Portilla, J. & Tabernero, A. (1998). Efficeint sapatial-domain implementation of a multiscale image representation based on Gabor functions. *Journal of Electronic Imaging,* Vol. 7, No. 1, pp. 166-173.
25. Schiele, B. & Crowley, J. (2000). Recognition without correspondence using multidimensional receptive field histograms. *Int. Journal of Computer Vision,* Vol. 36, No. 1, pp. 31-52.
26. Sangwine, S., Horne, R. (1998). *The color image processing handbook*. Chapman & Hall.
27. Duda, R., Hart, P. & Stork, D. (2000). *Pattern classification*. John Wiley & Sons.
28. Alpaydin, E. (2004). *Introduction to machine learning*. MIT Press.
29. Vapnik, V. (1995). The nature of statistical learning theory. Springer-Verlag.
30. Burges, J. (1998). A tutorial on support vector machines for pattern recognition, *Data Mining and Knowledge Discovery*, Vol. 2, No. 2, pp. 121-167.
31. Rantanen, V., Denessiousk, K., Gyllenberg, M., Koski, T. & Johnson, M. (2001). A fragment library based on Gaussian mixtures predicting favourable molecular interactions, *Journal of Molecular Biology*, Vol. 313, pp. 197-214.
32. Bishop, C. (1995). *Neural networks for pattern recognition*. Oxford University Press.
33. Nabney, I. (2002). Netlab algorithms for pattern recognition. Springer-Verlag.
34. Rabbani, H., Vafadoost, M. (2006). Wavelet based image denoising based on a mixture of laplace distributions, *Iranian Journal of Science and Technology, Transaction B, Engineering,* Vol. 30, No. B6, pp. 711-733.
35. Rissanen, J. (1983). A universal prior for integers and estimation by minimum description length, *Annals of Statistics,* Vol. 11, pp. 416-431.
36. Metz, C. (1986). ROC methodology in radiological imaging. *Investigate Radiology*, Vol. 21, pp. 720-733.